Hindawi
Shock and Vibration
Volume 2024, Article ID 9618500, 16 pages
https://doi.org/10.1155/2024/9618500

Research Article

Analysis of Wheel Wear and Wheel-Rail Dynamic Characteristics of High-Speed Trains under Braking Conditions

Rui Song,[1,2,3] Chenxu Lu ,[4] Lixia Sun,[5,6] Zhongkai Zhang,[3] Dilai Chen ,[4] and Gang Shen[1]

[1]*Railway and Urban Rail Transit Research Institute, Tongji University, Shanghai 201804, China*
[2]*China Railway Test and Certification Center Limited, Beijing 100081, China*
[3]*Standards and Metrology Research Institute of China Academy of Railway Sciences Corporation Limited, Beijing 100081, China*
[4]*School of Railway Transportation, Shanghai Institute of Technology, Shanghai 201418, China*
[5]*Railway Science and Technology Research and Development Center of China Academy of Railway Sciences Corporation Limited, Beijing 1000818, China*
[6]*Wheel-Rail System Laboratory, National Engineering Research Center of System Technology for High-Speed Railway and Urban Rail Transit, Beijing 1000818, China*

Correspondence should be addressed to Chenxu Lu; 18810327668@163.com and Dilai Chen; chendilai@163.com

Received 20 October 2023; Revised 5 January 2024; Accepted 13 January 2024; Published 25 January 2024

Academic Editor: Nicolo Zampieri

When high-speed trains operate under braking conditions, the wheel-rail interaction increases significantly, which can lead to more serious wear problems. To analyze the evolution of wheel wear and the dynamic characteristics of wheel-rail under braking conditions, this paper first carries out long-term monitoring of the service state of wheel-rail during the operation period. The study analyzed the matching characteristics of the measured wheel-rail profile and calibrated the wear model by using the collected data. The resulting wear prediction model was then used to examine the wheel wear characteristics under braking conditions. The research results indicate that during the operation period, the wheel experiences tread concave wear within a range of ±20 mm of the rolling circle, at a rate of approximately 0.05 mm per 10,000 km. Meanwhile, the rail experiences top surface wear at a natural rate of about 0.09 mm per year. Concave wear causes the contact point of the wheel-rail to appear in two zones, resulting in a sudden change of contact geometric parameters. The concave worn wheel and rail with a 60 N profile have better matching compared to the 60 rail profile. Increasing the braking torque and wheel-rail friction coefficient will significantly increase the wheel wear depth on straight sections. On small-radius curve sections, rail side lubrication can significantly reduce high rail side wheel flange wear. A worn concave wheel can lead to unfavorable wheel-rail contact geometry characteristics and increase low-frequency components in the vehicle's lateral dynamic response.

1. Introduction

By the end of 2022, the China's high-speed railway operating mileage has reached 42,000 kilometers, and the high-speed railway is becoming the preferred mode of transportation for more and more people. However, due to the high speed, short departure interval, and high traffic density of high-speed trains, frequent impacts occur between the wheels and the track, and the interaction between the wheel and the rail becomes more intense, and the wear and contact fatigue between the wheel and the rail also become more serious. Therefore, some problems caused by wheel-rail wear need to be paid attention to in the daily operation and management process of high-speed rail. It should be noted that when the train brakes and slows down, the interaction between the wheel and rail will increase significantly, which will lead to more serious wheel-rail wear. Therefore, the wheel-rail wear problem under braking conditions needs to be focused on.

Experts and scholars have conducted a lot of research and calculations on wheel-rail wear issues around material wear models, profile smoothing algorithms, and local contact theory. Luo et al. [1] established a coupling model of vehicle multibody system dynamics and wheel wear, and compared and analyzed the differences of the Archard wear

model, wear model based on friction work, and wear model based on wear index in predicting the development and distribution of high-speed rail wheel profile wear. Ding et al. [2] took the C80 freight car as the research object and analyzed the influence of axle load, speed, curve radius, and wheel hardness on wheel tread wear based on Pearce, Zobory, Jendel, and Braghin four wear models. Braghin et al. [3] proposed a USFD wear function, introduced it into the field of wheel-rail wear calculation, and verified the rationality of the model calculation by using a disc test. Tao et al. [4] established a high-speed train wheel wear prediction model that includes vehicle-track dynamic simulation, local contact solution, wheel wear calculation, and profile smoothing and updating strategy and verified the model with the measured data. Orlova and Boronenko [5] studied the influence of bogie-frame interaction mode on wheel wear by combining experiment and numerical simulation. Quan Sun et al. [6] studied the influence law of curve radius, superelevation, and speed on wheel-rail wear by calculating the dynamic behavior of freight cars. Han and Zhang [7] established a numerical model for predicting wheel wear based on measured wear data. Based on the least squares method, the polynomial fitting method was used to obtain a numerical prediction method for wear.

With the development of wheel-rail rolling contact theory, scholars began to introduce non-Hertzian contact into the simulation calculations of wheel-rail wear. Jin et al. [8] established a three-dimensional vehicle-track coupling dynamic model based on non-Hertzian contact between wheel and rail and studied the wheel wear situation when a vehicle passed through the curve. Yang et al. [9] used a modified non-Hertz contact algorithm to calculate the influence of curve superelevation on rail wear. Li et al. [10] used improved Kalker non-Hertzian theory to calculate wheel-rail contact wear. The results show that the non-Hertzian contact model is more reasonable for small-radius curve flange wear.

After conducting more extensive research, a more comprehensive understanding of wheel-rail wear has been achieved. This includes taking into account factors such as wheel-rail elasticity and random wheel-rail contact characteristics. Meinders et al. [11] established a vehicle rigid-flexible coupling model, considering wheelset elasticity, and explained the generation mechanism of wheel polygonization. Aceituno et al. [12] and Tao et al. [13] studied the influence of rail flexibility on wheel wear calculation. In order to predict the evolution of wheel wear more accurately, Hossein-Nia et al. [14] considered the random parameters of wheel-rail interaction in the whole process of wear prediction, such as random rail profile and track irregularity. Luo et al. [15] proposed a wheel-rail wear prediction model considering random factors and used the model to discuss the influence of random characteristics of rail profile and track parameters on wheel tread wear.

The studies mentioned above analyze wheel-rail wear primarily from a vehicle dynamics perspective. Some scholars have also adopted the finite element theory to examine changes in wheel-rail wear. Xiao et al. [16] studied the influence of friction coefficient on wheel-rail wear. The results show that the friction coefficient has a great influence on the contact area wear depth and wear distribution. Wang et al. [17] proposed a friction work calculation method based on finite element theory and analyzed the tread wear of high-speed trains.

Scholars have also analyzed the effect of worn wheels on wheel-rail static contact characteristics, vehicle dynamics, and wheel-rail contact fatigue. Wilson et al. [18] analyzed the relationship between tread concave wear and vehicle swaying instability. The results show that concave tread does not directly lead to vehicle swaying instability, but will aggravate vehicle lateral vibration. Li et al. [19] used multibody dynamics simulation software Simpack to compare the changes in vehicle operation safety index before and after wheel wear. Sawley et al. [20, 21] analyzed the changes of wheel-rail contact geometry, wheelset yaw angle, and lateral force with wheel concave wear by using experimental and simulation analysis techniques. Lu et al. [22] tested the wheel-rail wear of the subway, analyzed the wheel-rail contact geometric relationship between the measured profile and the rail, and used the multibody dynamics software to study the influence of wheel wear on vehicle dynamic performance and wheel-rail contact damage characteristics. Jin et al. [23] systematically analyzed and summarized the lateral wear situation, characteristics, formation mechanism, and influence on vehicle dynamic behavior of high-speed railway.

In addition, wear management is carried out from the two perspectives of wheel-rail friction management and profile optimization. Ignesti et al. [24, 25] proposed a wear model that can simultaneously predict the wheel-rail profiles on small-radius curves and then gave a method for optimizing the design profiles of wheel-rail. Ishida et al. [26] found that wheel-rail friction management can significantly optimize wheel-rail dynamic interaction and greatly reduce lateral wheel-rail force and wheelset yaw angle when a vehicle passes through a curve by numerical simulation and field test. Wear caused by rail turns out to be a problem.

The abovementioned studies have conducted a more detailed study on the mechanism of wheel-rail wear, the influence of wheel-rail wear on the wheel-rail contact geometry, and the dynamic performance of the wheel-rail system; however, in the research on wheel-rail wear, train acceleration and deceleration conditions are rarely considered. In the process of train operation, there are often situations such as braking, and the large wheel-rail creep caused by braking will affect the wheel-wear simulation results. Therefore, based on the consideration of train braking action, this paper establishes a wheel wear prediction model and calibrates the model with the measured data. By using the numerical model, the influence law of braking torque, friction coefficient, and running speed on the distribution and development of wheel wear of high-speed trains is studied, in order to provide guidance and reference for wear management and track maintenance in high-speed train operation.

2. Wheel-Rail Service Status of Long-Term Monitoring

2.1. Introduction to Field Testing. In order to understand the relationship between wheel-rail profile status and the service time of the wheel-rail system, this paper selects the Beijing-Shanghai high-speed railway as a typical line and carries out long-term monitoring on the wheel and rail profiles, as shown in Figure 1. The profile calibration algorithm is used to preprocess the measured profile data [27]. Combined with the observed profile data, statistics and wheel-rail matching analysis are carried out to study the change of wheel-rail profile in the service process and to further evaluate the distribution of wheel-rail contact points under different service conditions.

2.2. Wheel Service Status. Figures 2 and 3 show the changes in the reprofiled LMB10 wheel profile over time. It can be seen from the figures that the wheel mainly suffers from tread concave wear, and the wear distribution is within the −20~20 mm range of the tread; the wear distribution characteristics of the left and right wheels are basically consistent, and the maximum wear value occurs near the rolling circle of the wheelset. With the increase in running mileage, the wear range and depth gradually increase; the average wheel wear is basically linear with the operating mileage, and the wear rate is about 0.05 mm/10,000 km. With the increase in service time, the dispersion of wheel wear of the whole train gradually increases. Taking 100,000 km as an example, the maximum wear depth is 0.71 mm and the minimum wear depth is 0.42 mm.

Equivalent conicity is an important parameter to evaluate the matching of wheel-rail profiles. The UIC 519 standard method is used to calculate the equivalent conicity for a 3 mm amplitude. When wheels with different profiles are matched with the 60 rail profile and the 60 N rail profile [28], their equivalent conicities are calculated, respectively. It is evident from Figure 4 that the equivalent conicity of the wheel varies when matched with rails of different profiles. As the operating mileage increases, the equivalent conicity for the standard 60 rail exhibits a consistent linear growth trend, whereas the equivalent conicity for the 60 N rail initially increases before stabilizing gradually. During the initial stages of wheel reprofiling, the equivalent conicity of the wheels for both types of rails is almost the same. However, after operating for 100,000 kilometers, the 60 N rail exhibits better wheel-rail profile-matching performance, with an equivalent conicity of approximately 0.22. On the other hand, the standard 60 rail's equivalent conicity measures approximately 0.35, approaching the limit value corresponding to the lateral shaking alarm of the bogie [29].

Figures 5 and 6 show the wheel-rail profile-matching performance of different wheel profiles. The contact points on the wheel tread and rail profile are evenly distributed during the initial stage of wheel reprofiling. However, after concave wear occurs on the wheel, the distribution of contact points displays a zoning phenomenon, resulting in the distribution of wheel-rail contact points in two discontinuous regions. Upon further analysis, it was observed that after wheel reprofiling, the contact point position, rolling circle radius difference, and contact angle difference change smoothly as the wheelset moves laterally during the initial stage. However, in the case of a concave worn wheel, the contact point's position and contact geometric parameters exhibit a step pattern with lateral wheelset movement. The reason for this occurrence is that the wheel and rail lose contact at the concave wear center position, causing an abrupt shift in the contact point when the wheelset is laterally displaced. As a result, the contact geometric parameters also undergo sudden changes.

2.3. Rail Service Status. A long-term monitoring of the operating line was conducted to analyze the rail profile's performance. The results are presented in Figure 7. The analysis indicates that the rail's top wear depth and wear rate are both minimal, and there are some variations in the test data across different rail sections. Overall, the wear depth has an almost linear relationship with the service time, and the rail's average natural wear rate is approximately 0.09 mm/year.

An additional analysis was conducted on the measured rail profile deviations. The deviations were calculated for the rail top in relation to the 60 N reference profile [30]. Profiles were classified based on their deviation at a distance of 20 mm from the working edge. For example, 60 N_0.8 represents a deviation of 0.8 mm, and 60 N_−0.4 represents a deviation of −0.4 mm. The results of the rail profile deviation analysis are presented in Figures 8 and 9. The results illustrate a significant deviation between the nonworking side (−30~−10 mm) and the working side (10~30 mm), with a maximum deviation of 3.3 mm. At a distance of 20 mm from the working edge, the deviation value shows a normal distribution ranging from −0.4 mm to 0.8 mm, with approximately 60% of the deviation values falling within the range of 0~0.4 mm.

Figures 10 and 11 show the matching of different profile rails with new wheels. From the figures, it can be seen that as the wheelset moves laterally, the contact point position basically changes linearly. Among them, the rail contact point corresponding to 60 N_0.8 moves to the working edge side of the rail, while the rail contact point corresponding to 60 N_−0.4 moves to the rail top; the contact point position corresponding to 60 N_−0.4 rail profile is similar to the 60 N rail profile.

Figure 12 displays the equivalent conicity of a wheel when matched with different rail profiles. The results show that for a reprofiled wheel, the equivalent conicity is approximately 0.1 when the wheelset lateral displacement is less than 9 mm. However, when the lateral displacement exceeds 9 mm, the equivalent conicity increases rapidly. When dealing with concave worn wheels, the equivalent conicity can be divided into three stages based on the lateral displacement. In the range of 0~5 mm, the equivalent conicity shows a trend of first rising and then falling, among which the equivalent conicity corresponding to 60 N_0.8 is larger, even exceeding the limit

(a) (b)

Figure 1: Wheel-rail profile of long-term monitoring in Beijing-Shanghai high-speed railway. (a) Wheel profile. (b) Rail profile.

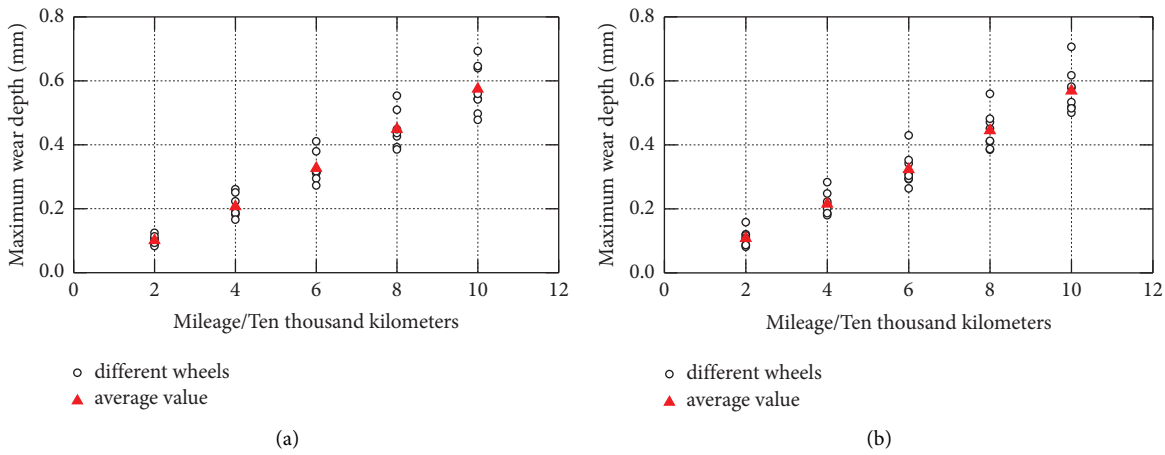

(a) (b)

Figure 2: Wheelset wear depth under different operating mileage. (a) Left wheel. (b) Right wheel.

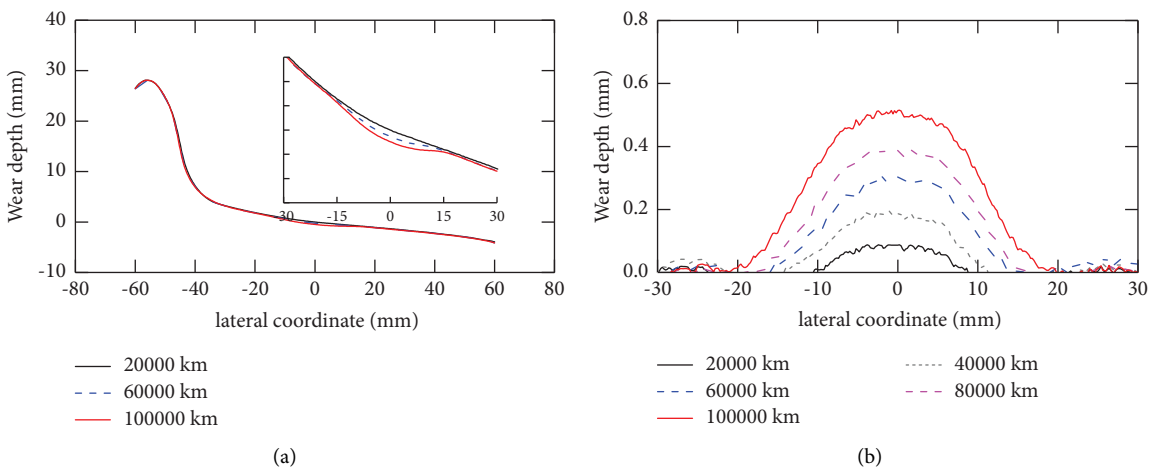

(a) (b)

Figure 3: Wheelset wear distribution under different operating mileage. (a) The worn wheel. (b) Wear distribution.

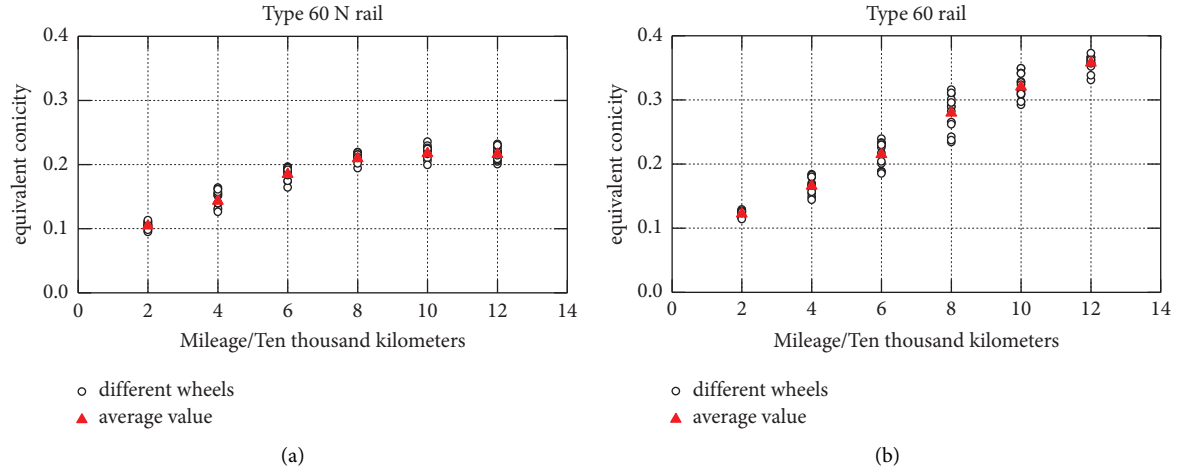

Figure 4: Equivalent conicity of different worn wheels. (a) Type 60 N rail. (b) Type 60 rail.

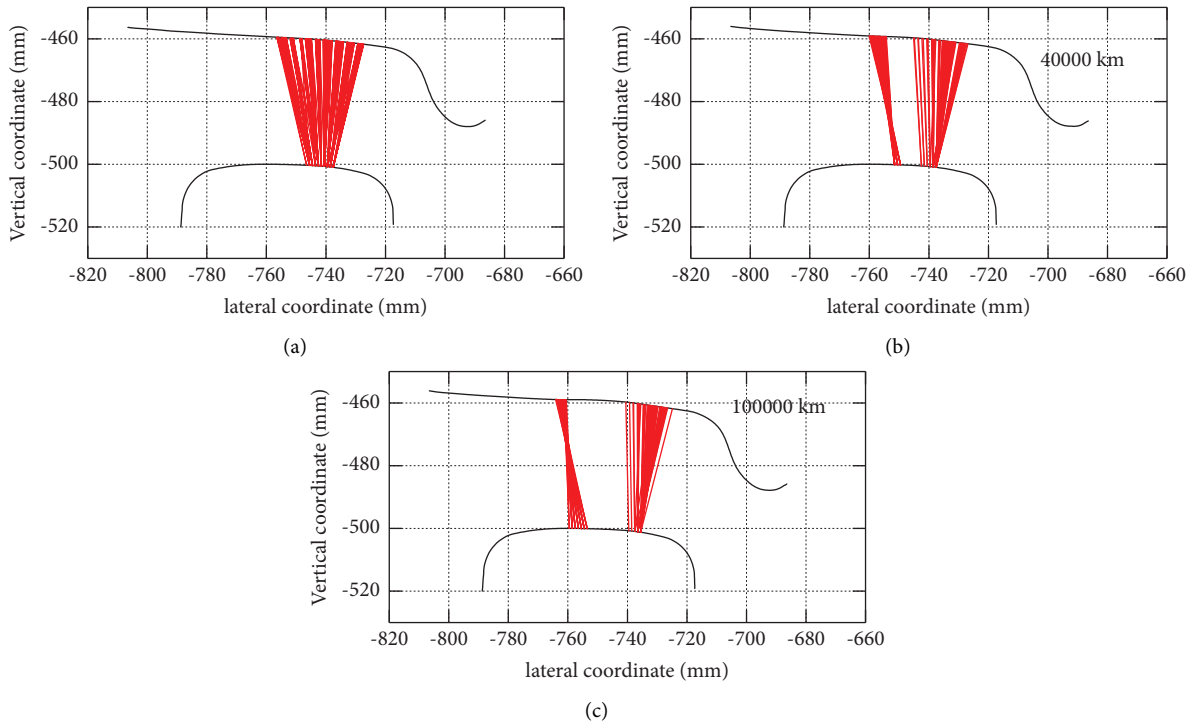

Figure 5: Distribution of contact points. (a) Initial stage of reprofiled wheel. (b) 40000 km. (c) 100000 km.

value of 0.35; while the equivalent conicity corresponding to 60 N_−0.4 is smaller, which may cause low-frequency oscillation of the car body [29], in the range of 5~10 mm, the difference of equivalent conicity corresponding to different profile rails is small and shows a slow downward trend; after exceeding 10 mm, the equivalent conicity rises rapidly and shows differentiation.

3. Model Construction

3.1. Vehicle-Track Dynamic Interaction Model. The study focuses on the high-speed vehicle equipped with a reprofiled LMB10 wheel profile. A 42-degree-of-freedom coupled dynamic model of the vehicle in lateral-vertical-longitudinal directions is established using multibody system dynamics theory [31]. The model consists of one car body, two bogies, and four wheelsets, which are connected by primary and secondary suspensions, as shown in Figure 13. The primary suspension employs an axle box arm positioning device and features vertical springs and damping mechanisms. The secondary suspension utilizes air spring support and is equipped with antiyaw dampers, lateral hydraulic dampers, and lateral rubber bumpers.

In this paper, the track structure is appropriately simplified and simulated by using a single-layer track model. As shown in Figure 14, the model considers the elastic bending

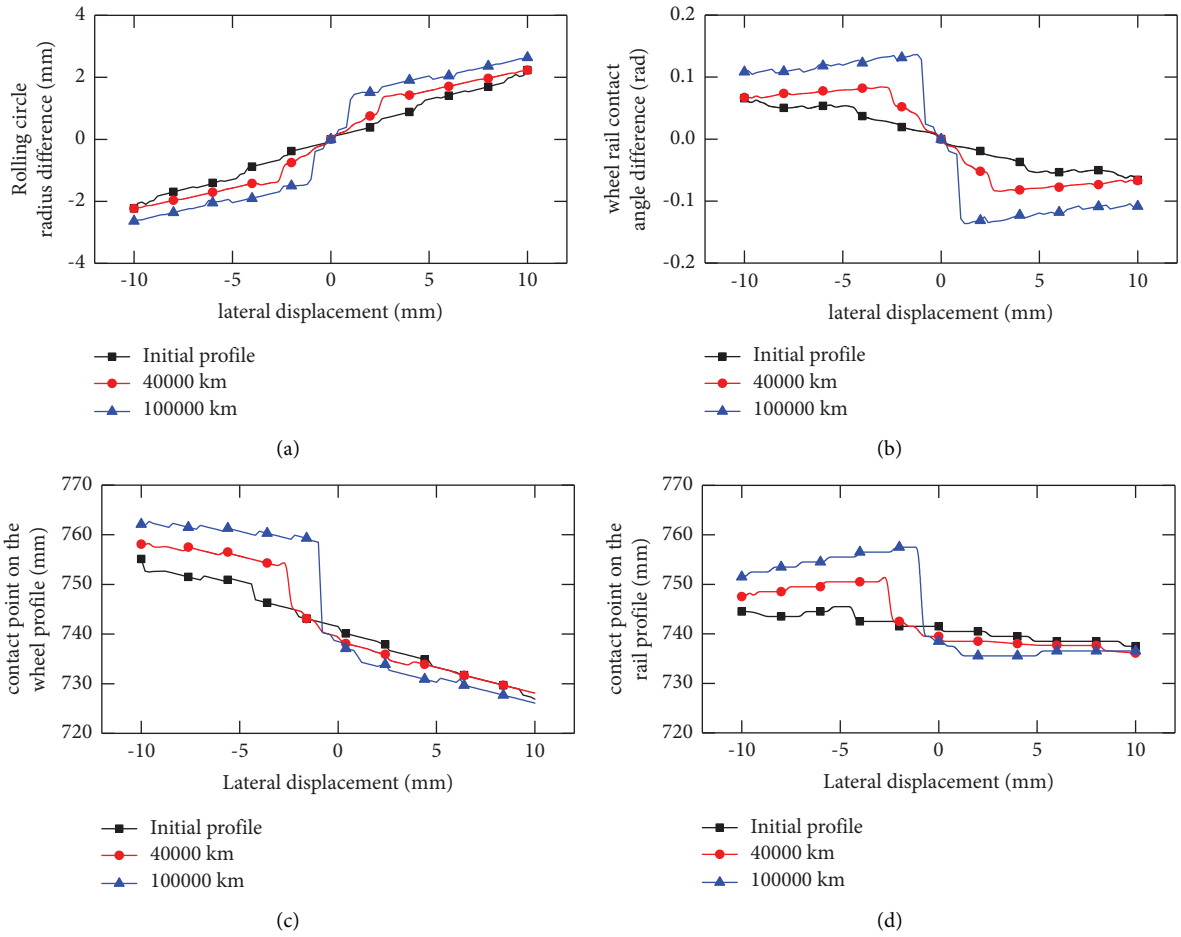

Figure 6: Wheel-rail contact geometry parameters. (a) Rolling circle radius difference. (b) Wheel-rail contact angle difference. (c) Contact position on the wheel profile. (d) Contact point on the rail profile.

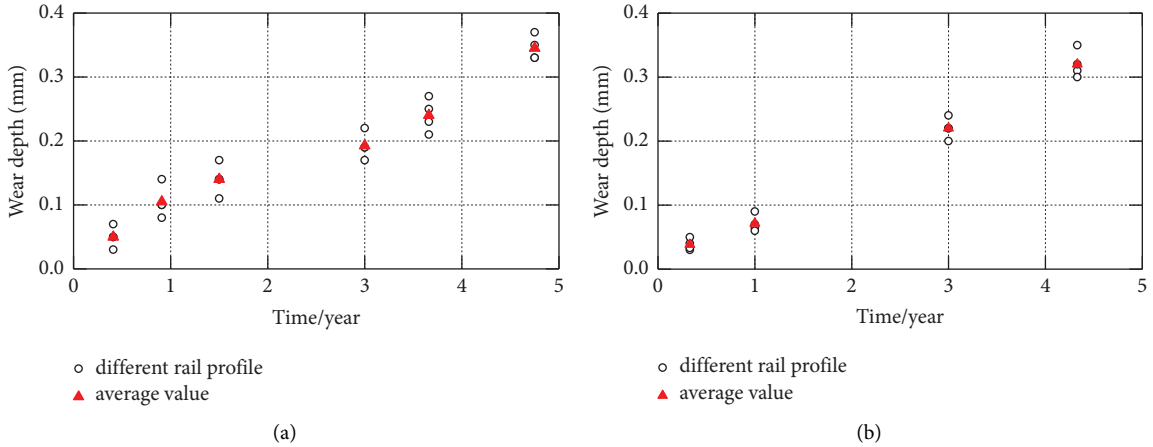

Figure 7: Rail wear rate. (a) Measuring point 1. (b) Measuring point 2.

of the rail and treats the rail as a spatial beam model supported by discrete flexible supports. The deformation displacements of the left and right rails are independent of each other; the vertical deformation displacement and the lateral deformation displacement are independent of each other. A three-directional spring-damper element is used to simulate the vertical, lateral, and longitudinal constraint characteristics of the fastener.

The vehicle subsystem and the track subsystem are constructed by using the MATLAB development platform and coupled by the wheel-rail contact relationship. The FASTSIM algorithm [32] is adopted in the paper for the

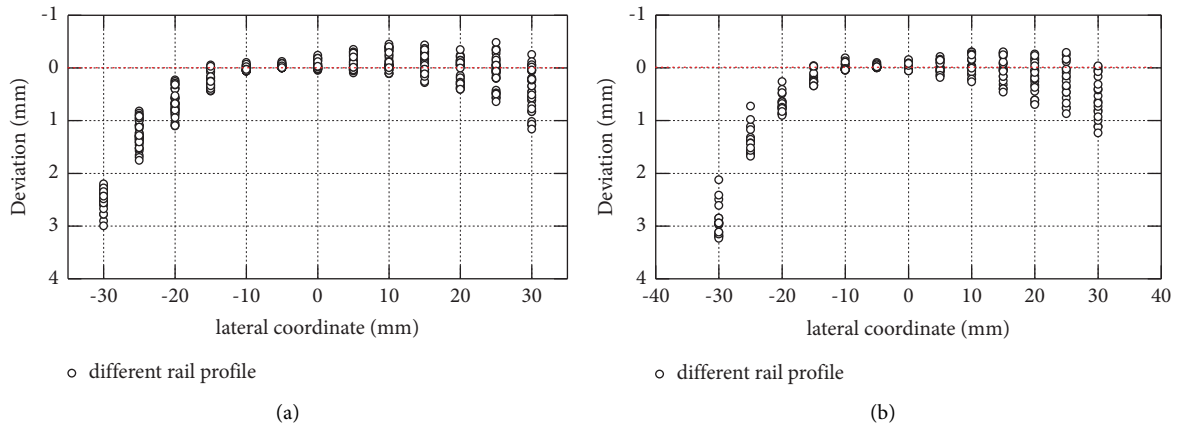

Figure 8: Measured rail profile deviation (compared with the 60 N rail profile). (a) Left rail. (b) Right rail.

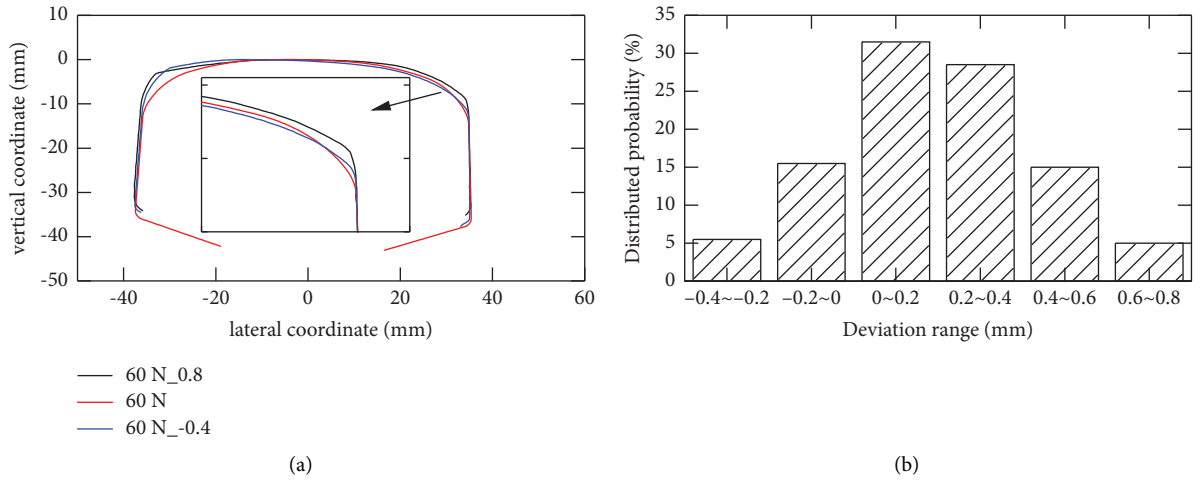

Figure 9: Rail profile and deviation distribution. (a) Different rail profiles. (b) Rail profile deviation distribution (20 mm from the working edge).

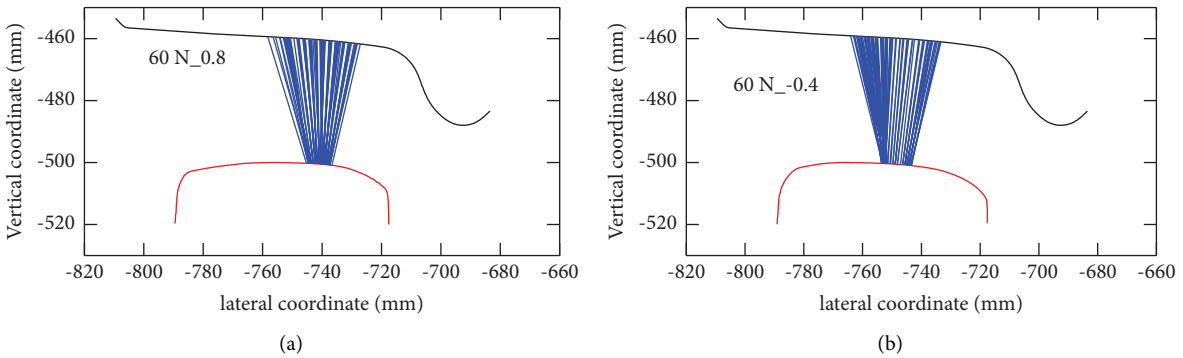

Figure 10: Distribution of wheel-rail contact points with different rail profiles. (a) 60 N_0.8. (b) 60 N_−0.4.

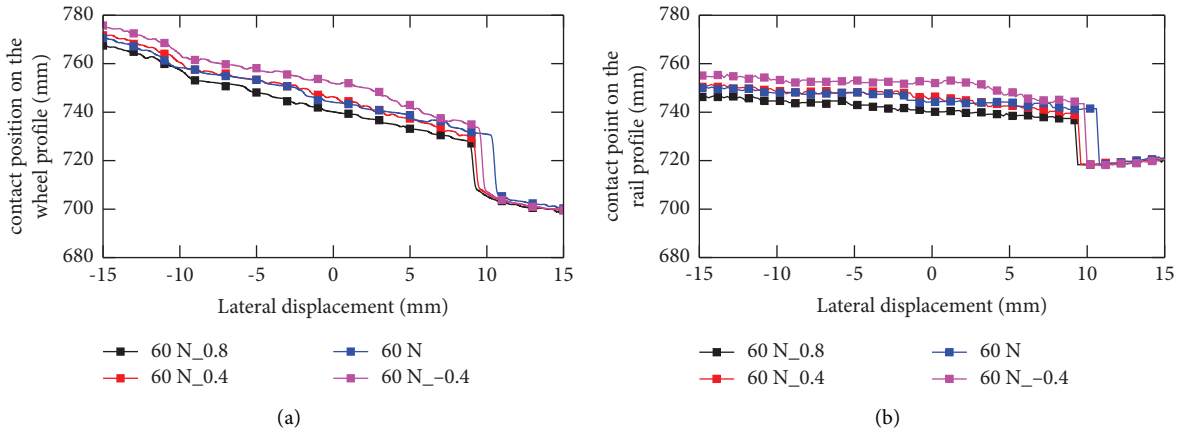

Figure 11: Lateral position of the wheel-rail contact point under different wheelset lateral displacements. (a) Contact point on the wheel profile. (b) Contact point on the rail profile.

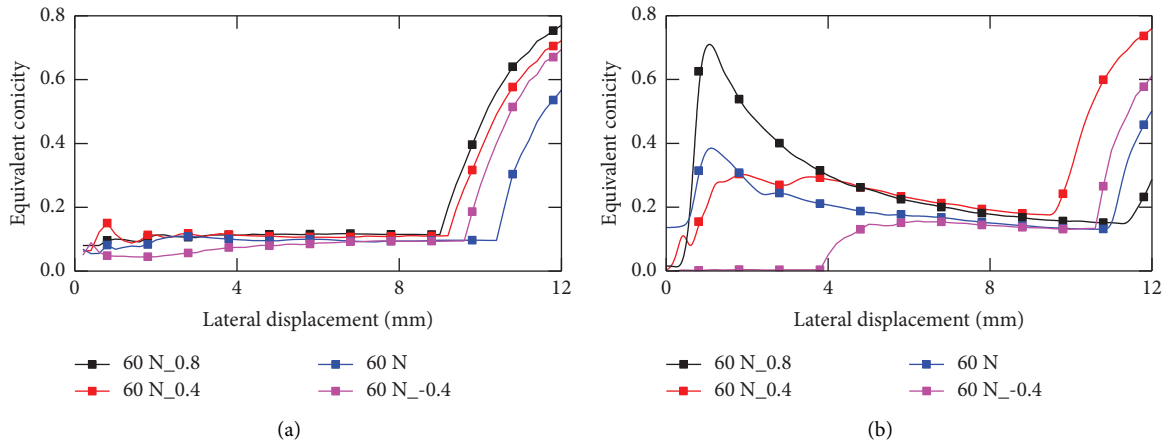

Figure 12: Equivalent conicity of the wheel when matched with different rail profiles. (a) Reprofiled wheel. (b) 100,000 km after wheel reprofiling.

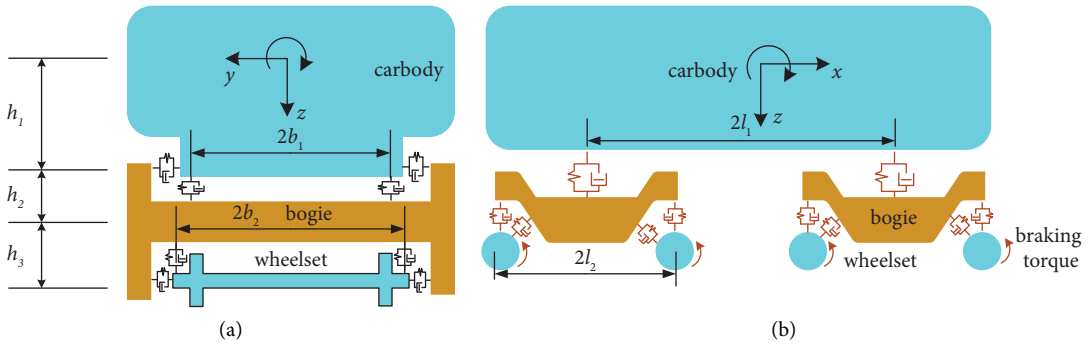

Figure 13: The vehicle model. (a) Side view. (b) Front view.

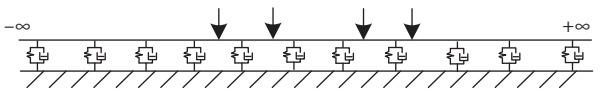

Figure 14: The track model.

wheel-rail rolling contact analysis. In this algorithm, the elliptical contact patch is divided into independent longitudinal parallel strips, each strip is divided into the same number of elements (as shown in Figure 15), and a chain solution is performed along the rolling direction from the front edge of the contact patch.

The creepage and creep force at the center point of the element are adopted for the values of each element. Then, the stress distribution at the center point is determined as

$$\begin{cases} p_x(x, y_i) - p_x(x - \mathrm{dx}, y_i) = \dfrac{\xi_x \mathrm{dx}}{L_1} - y_i \dfrac{\xi_{\mathrm{sp}}}{L_3} \mathrm{dx}, \\ p_y(x, y) - p_y(x - \mathrm{dx}, y_i) = \dfrac{\xi_y \mathrm{dx}}{L_2} + \dfrac{\xi_{\mathrm{sp}}}{2L_3}(x + a_i)\mathrm{dx}, \\ p_z(x, y) = \dfrac{3N}{2\pi \mathrm{ab}} \sqrt{1 - \left(\dfrac{x}{a}\right)^2 - \left(\dfrac{y}{b}\right)^2}, \end{cases} \tag{1}$$

where p_x is the traction in the x direction, p_y is the traction in the y direction, p_z is normal pressure, L_1, L_2, and L_3 are the flexibilities of the simplified theory, and a_i represents the x-coordinate of the front edge for the ith strip in the contact patch.

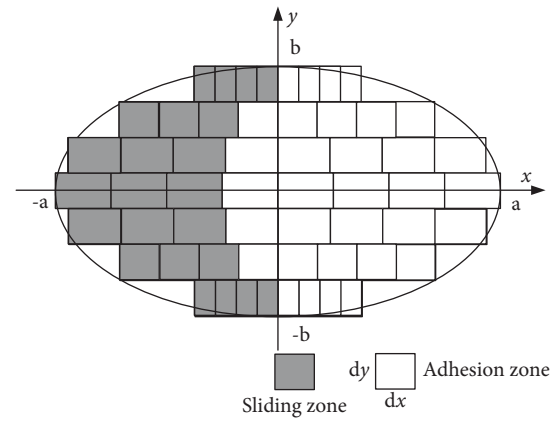

Figure 15: The contact patch.

For the tangential stress at each element, the creep forces are calculated from the front edge to the rear edge of the contact patch and are solved iteratively. According to Coulomb's friction law, it is determined whether the element belongs to the sliding zone or the adhesive zone. As a result, the element stress within the contact patch is divided into two categories.

$$\begin{cases} p_x' = p_x, p_y' = p_y, & \sqrt{{p_x}^2 + {p_y}^2} \le \mu p_z, \\ p_x' = \dfrac{p_x}{\sqrt{{p_x}^2 + {p_y}^2}} \mu p_z, p_y' = \dfrac{p_y}{\sqrt{{p_x}^2 + {p_y}^2}} \mu p_z, & \sqrt{{p_x}^2 + {p_y}^2} > \mu p_z, \end{cases} \tag{2}$$

where μ is the friction coefficient.

3.2. Wear Simulation Process. Wheel-rail wear models can establish the relationship between the rolling contact parameters and material wear at the wheel-rail interface. Based on bench tests, scholars at home and abroad have proposed various wear prediction models, among which the Archard model and the Zobory model are more commonly used [33]. The Archard adhesive wear model has achieved good results in the simulation of wheel-rail wear of high-speed trains, so this paper chooses the Archard model to calculate the material loss of the discrete elements in the sliding zone (as shown in Figure 16), which is expressed as follows:

$$V_{\mathrm{wear}} = k_{\mathrm{w}} \frac{\mathrm{Nd}}{H}, \tag{3}$$

where $\mathrm{V_{wear}}$ (unit: $\mathrm{m^3}$) is the material wear volume, d (unit: m) is the sliding distance, N (unit: N) is the normal force, H (unit: Gpa) is the material hardness of the softer object in the two contacting objects, and k_{w} is the wear coefficient.

Jendel [34] gave the relationship between the wear coefficient, contact stress, and sliding speed, as shown in Figure 17. According to the variation of sliding speed and contact pressure, the wear coefficient can be divided into 4 zones: zone I is the heavy wear area, and the value is $300 \times 10^{-4} \sim 400 \times 10^{-4}$; zone II and IV are light wear areas, and the wear coefficient ranges from 1×10^{-4} to 10×10^{-4}; zone III is a moderate wear area, and the wear coefficient is $30 \times 10^{-4} \sim 40 \times 10^{-4}$. By changing the wear coefficients in different zones, and comparing the simulation results with the measured data. After testing, the appropriate wear coefficient values in the wear model are $k_1 = 3.1 \times 10^{-3}$, $k_2 = 5.2 \times 10^{-5}$, $k_3 = 3.1 \times 10^{-4}$, and $k_4 = 5.2 \times 10^{-5}$.

According to Kalker's simplified theory, the wear depth of any element in the wheel-rail contact patch sliding area can be expressed as follows:

$$\triangle z(x, y) = \frac{k_{\mathrm{w}} p_z d}{H}, \tag{4}$$

where d denotes the wheel sliding distance within time increment Δt, which can be obtained as follows:

$$d = \sqrt{s_x^2 + s_y^2} \Delta t = \sqrt{s_x^2 + s_y^2} \, \frac{\mathrm{dx}}{vc}, \tag{5}$$

$$\begin{aligned} s_x(x, y) &= v_c\left(\xi_x - \xi_{\mathrm{sp}} y\right), \\ s_y(x, y) &= v_c\left(\xi_y + \xi_{\mathrm{sp}} y\right), \end{aligned} \tag{6}$$

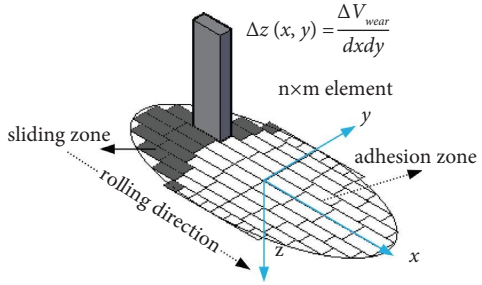

Figure 16: Wear depth in the contact patch.

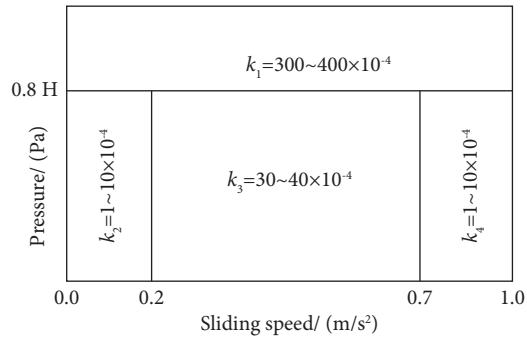

Figure 17: Wear coefficient map.

where s_x and s_y (m/s) represent the longitudinal and lateral sliding speeds, ξ_x and ξ_y represent the longitudinal and lateral creepages, ξ_{sp} represents the spin creepage, v_c (m/s) represents the speed of the wheel passing through the contact patch, and dx (m) represents the length of the contact patch discretization element.

By substituting equations (5) and (6) into equation (4), the wear depth can be obtained as follows:

$$\triangle z(x, y) = \frac{3\mathrm{Nk_w}}{2\pi \mathrm{abH}} \sqrt{1 - \left(\frac{x}{a}\right)^2 - \left(\frac{y}{b}\right)^2} \sqrt{s_x^2 + s_y^2}\ \frac{\mathrm{dx}}{v_c}. \quad (7)$$

By using the abovementioned calculation, the wear depth of each discrete element in the contact patch can be obtained, and then the wear depth of the sliding zone discrete elements is superimposed and projected onto the wheel-rail profile along the wheel rolling direction, which can obtain the wear depth distribution of the wheel rolling one circle. The wheel wear prediction simulation program includes a vehicle-track dynamics simulation module, a wear depth calculation module based on the wheel wear model, and a profile update module. The flow chart is shown in Figure 18. When calculating the wear depth of a contact patch, the wear depth calculation module first divides the contact patch into $n \times m$ elements according to the wheel-rail creepage and contact geometry, calculates the vertical wear depth of each element in the contact patch, accumulates along the wheel rolling direction to obtain the vertical wear depth of the whole contact patch, and then projects it onto the wheel profile to obtain the wheel profile wear depth. Since it is difficult for dynamic simulation to update the wheel profile in real time, it is necessary to set up a profile

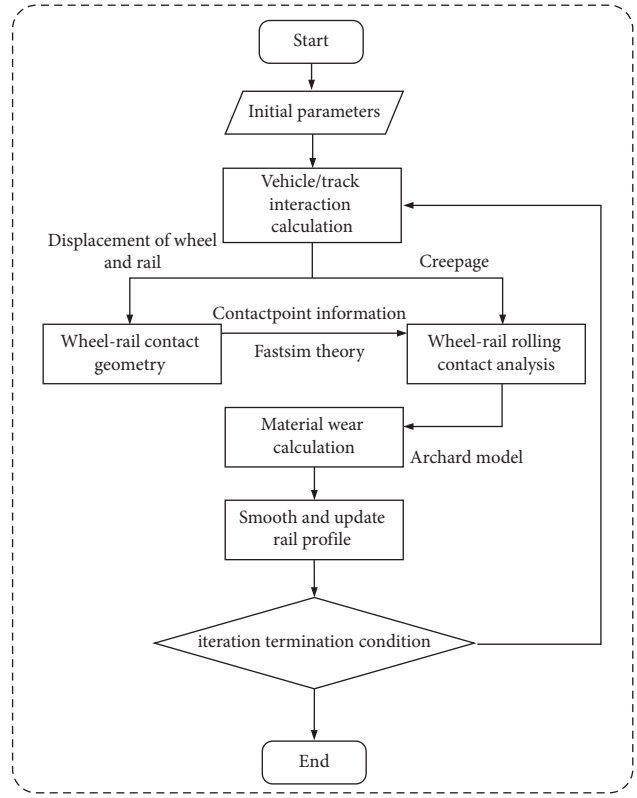

Figure 18: The calculation process of wheel wear.

update strategy to ensure the accuracy of the results as much as possible. In this paper, the profile is updated when the wear depth reaches 0.1 mm.

3.3. Model Verification. To verify the accuracy of the wheel-rail wear simulation analysis platform built in this paper, the simulation results and the actual measurement results of the high-speed train are compared and analyzed, and the wear coefficient in the Archard wear model is adjusted according to the measured results. The calculation results are shown in Figure 19, and the analysis shows that the simulated and measured profiles are basically close. After the vehicle runs 40,000 km, the simulated wear depth is 0.19 mm, and the measured data is 0.2 mm; after the vehicle runs 80,000 km, the simulated wear depth is 0.42 mm, and the measured data is 0.40 mm, with relative errors of less than 5%.

4. Analysis of Wheelset Wear Characteristics under Braking Conditions

4.1. Brake Torque. When a train passes through a speed-limited section in actual operation, it often needs to activate the braking mode, and different braking levels are adopted according to the actual situation, which means applying different braking torques. In order to investigate the influence of different braking levels on wheel wear, the vehicle decelerates and runs for 1,000 m with different braking torques, and the cumulative mileage is 50,000 km. Three

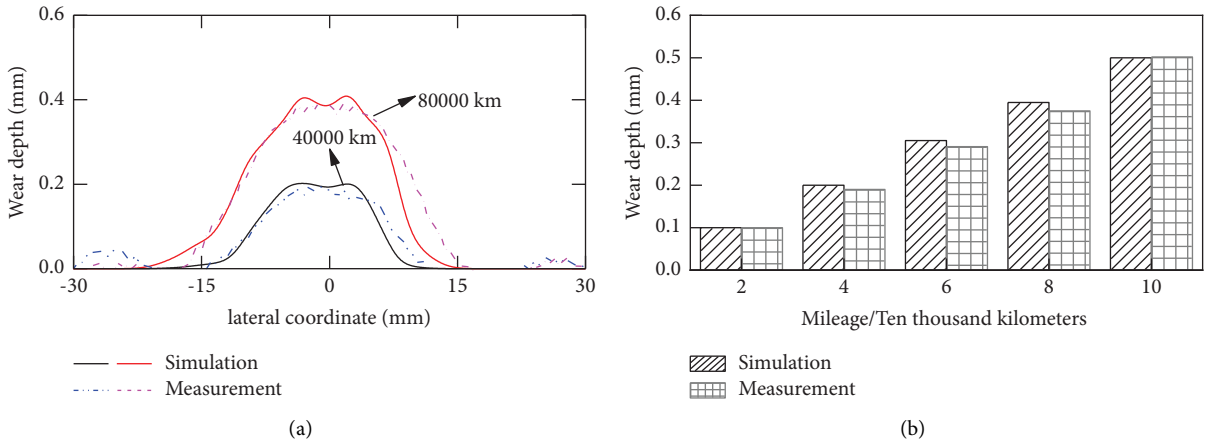

Figure 19: Wheel wear distribution and wear maximum depth. (a) Wear distribution. (b) Wear depth.

braking conditions of 2, 3, and 4 kN m per wheelset are considered and the friction coefficient is 0.3.

Figure 20 displays the distribution of wheel wear and longitudinal creepage variation under different braking torques. The wear is distributed within ±20 mm of the nominal rolling circle of the wheel profile, regardless of the braking torque. However, the wear depth increases with the increase in braking torque. Specifically, the wear depth almost doubles when the braking torque increases from 2 kN·m to 4 kN·m. When braking, the wheel-rail longitudinal creep becomes positive, causing the wheel's actual forward speed to exceed its pure rolling forward speed. The greater the braking torque, the greater the wheel-rail slip, which leads to increased wheel wear. Therefore, wear and braking time are in conflict. Increasing the braking torque can result in greater deceleration and a reduction in braking time. However, it will also result in increased wheel wear, which will worsen the wheel-rail interaction relationship.

4.2. Friction Coefficient. In order to study the influence of different rail surface conditions on wheel wear during train braking, two cases are considered: rail top lubrication on a straight section and rail side lubrication on a small-radius curve section. Different friction coefficients are set in the simulation to represent different rail surfaces, where the friction coefficient of a normal rail surface is 0.3 and the friction coefficient of a lubricated rail surface is 0.1. After the rail surface is lubricated, the wear coefficient is reduced by about half [35].

Figure 21 shows the wheel wear distribution and adhesion-slip distribution under different friction coefficients on a straight section. It can be seen from the figure that lubrication of the rail surface has a greater effect on wheel wear and the distribution of the stick-slip zone in the contact patch. Wheel wear depth is reduced by about 23% and the proportion of sliding areas is increased by almost 2 times. Overall, although the reduction in the coefficient of friction causes greater creep, the reduction in the coefficient of wear has a more obvious effect on wheel wear.

Figures 22 and 23 show the influence of rail side lubrication on wheel wear on a small-radius curve section, with a running mileage of 5000 km. The analysis shows that the wheel wear on the left and right sides of the small-radius curve section shows differentiation, with wheel flange wear in the range of 20~40 mm on the high rail side and tread wear in the range of −35~10 mm on the low rail side. Rail side lubrication has little effect on the low rail side and mainly affects the wheel flange wear on the high rail side. Under lubrication conditions, the maximum wear depth can be reduced from 0.55 mm to 0.23 mm. This is because the outer side of the small-radius curve section mainly relies on wheel flange guidance, and rail side lubrication can effectively reduce the vehicle curve passing force, thus effectively reducing the wheel flange wear.

4.3. Running Speed. Figure 24 shows the influence of vehicle running speed on wheel wear. It can be seen from the figure that different initial braking speeds have little effect on the wear distribution range, but they mainly affect the wear depth. When the speed increases from 150 km/h to 350 km/h, the wear depth increases by 25%. This is because under the influence of track irregularity, the lateral swing amplitude of the wheelset will increase when the train runs at a higher speed, and the tangential force and sliding speed will also increase accordingly; the wheel-rail relative sliding distance will also increase further, which undoubtedly aggravates the wheel wear.

5. Influence of Wheel Wear on Vehicle Dynamic Behavior

Wheel tread concave wear alters the geometry of the wheel-rail contact, which affects the vibration characteristics of the wheel-rail coupling system. This section compares and analyzes the influence of wheel wear on vehicle dynamic behavior by selecting the original wheel profile and the concave worn wheel with a wear depth of 0.5 mm. Figure 25 illustrates the changes in wheel-rail dynamic performance before and after wheel wear. The figure illustrates that

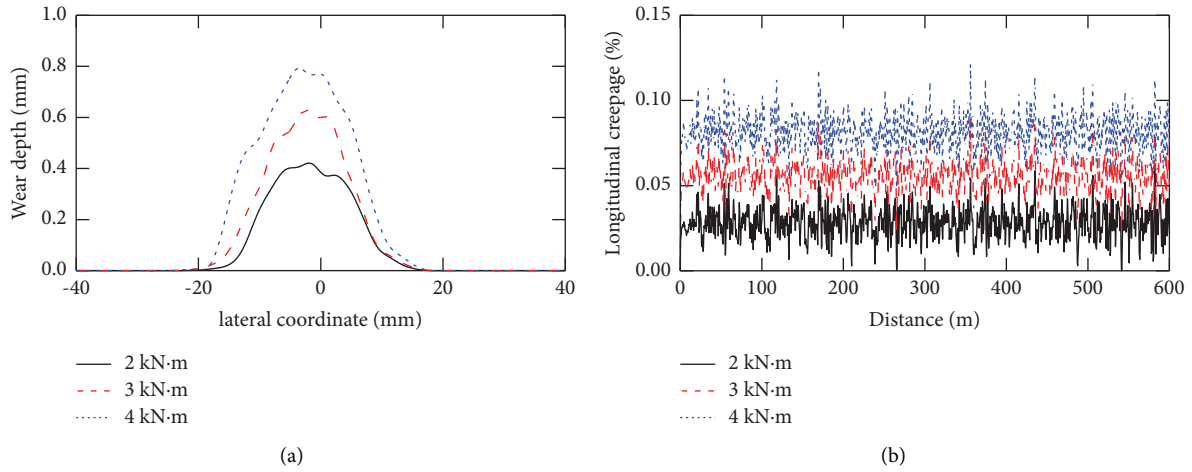

Figure 20: The wheel wear distribution and longitudinal creepage under various braking torques. (a) Wear distribution. (b) Longitudinal creepage.

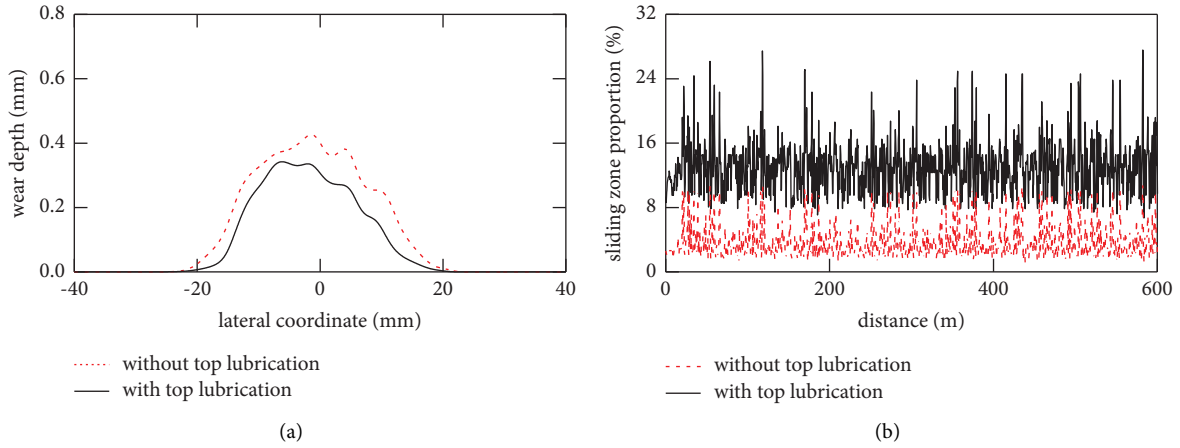

Figure 21: The wear distribution and sliding zone proportion under different rail top conditions. (a) Wear distribution. (b) Sliding zone proportion.

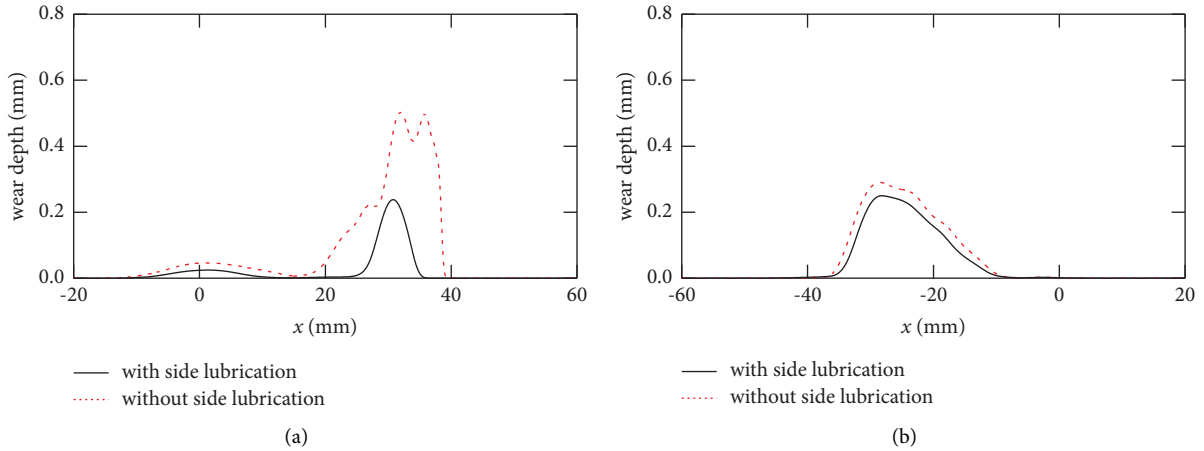

Figure 22: The wheel wear distribution under different rail side conditions. (a) High rail side. (b) Low rail side.

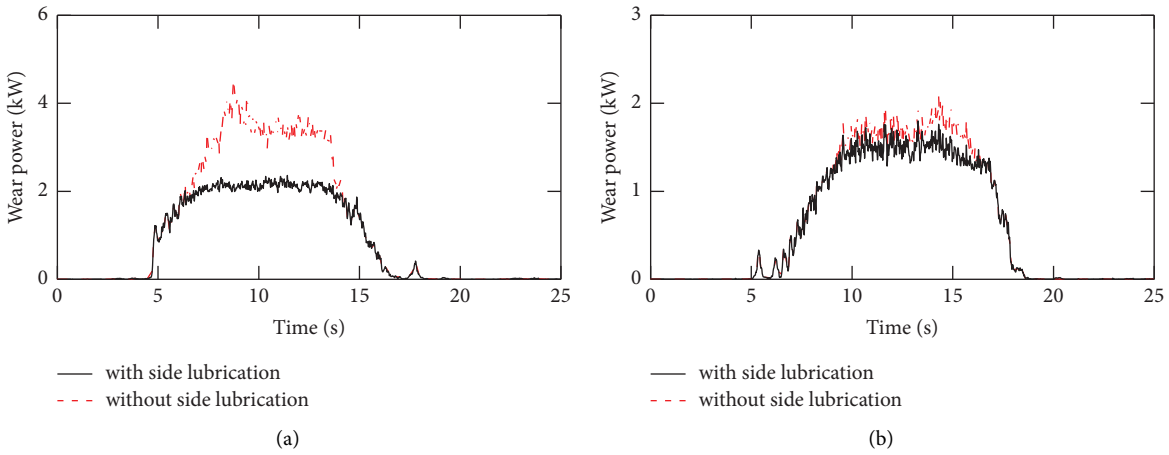

Figure 23: The wheel wear power under different rail side conditions. (a) High rail side. (b) Low rail side.

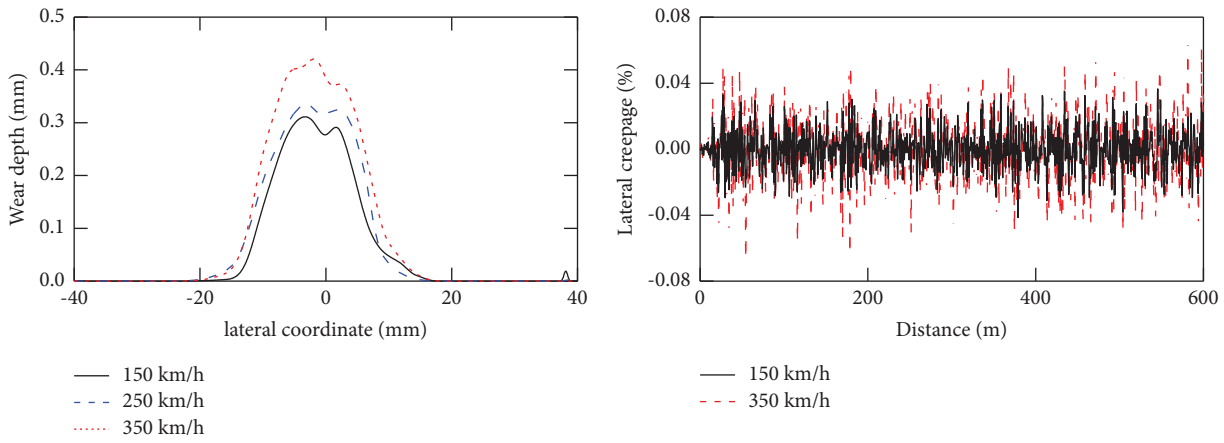

Figure 24: Wheel wear distribution and lateral creepage with various running speeds. (a) Wear distribution. (b) Lateral creepage.

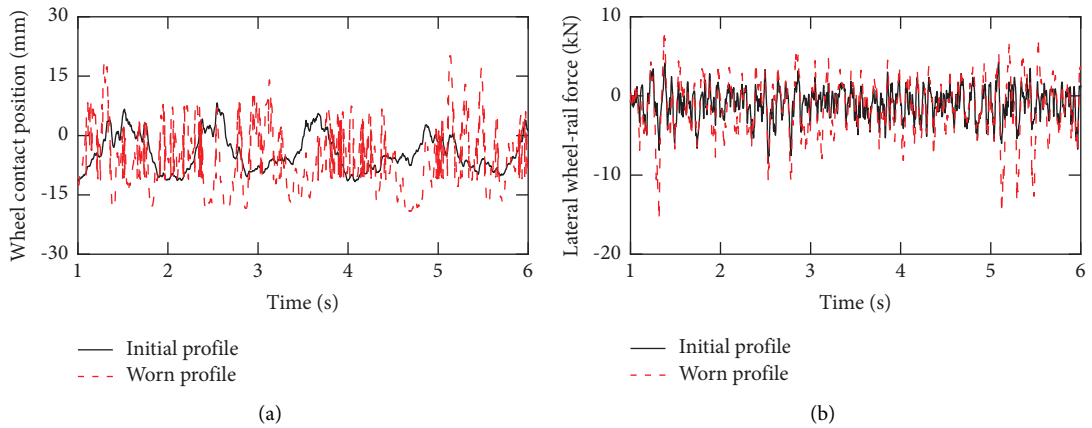

Figure 25: The wheel-rail dynamic behavior before and after wheel wear. (a) Position of the wheel contact point. (b) Lateral wheel-rail force.

concave wear results in a stronger lateral oscillation of the wheelset, causing significant fluctuations in the wheel-rail lateral force.

Figures 26 and 27 display the lateral dynamic response and comfort index of the vehicle before and after wheel wear. The figures indicate that the wheel concave wear leads to

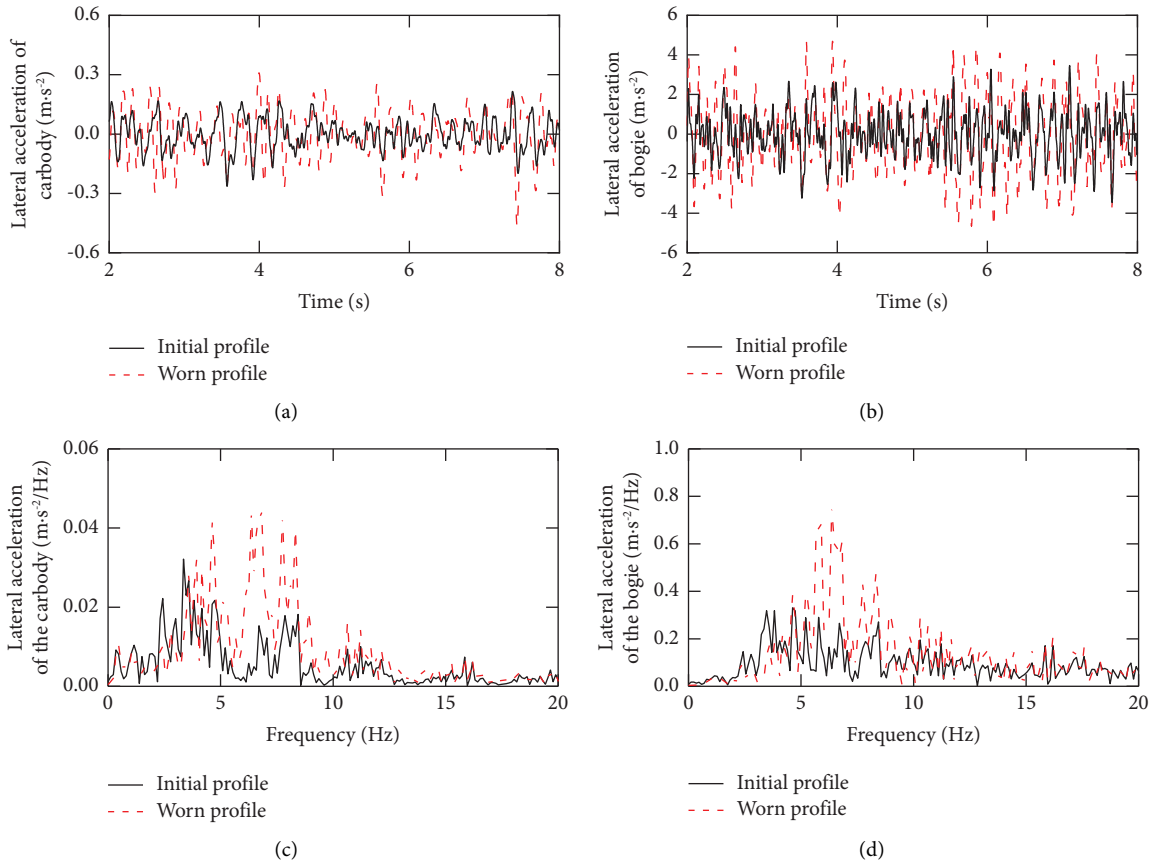

Figure 26: Dynamic performance of the vehicle before and after wear. (a) Lateral acceleration of the car body. (b) Lateral acceleration of the bogie. (c) Spectrum of lateral acceleration of the car body. (d) Spectrum of lateral acceleration of the bogie.

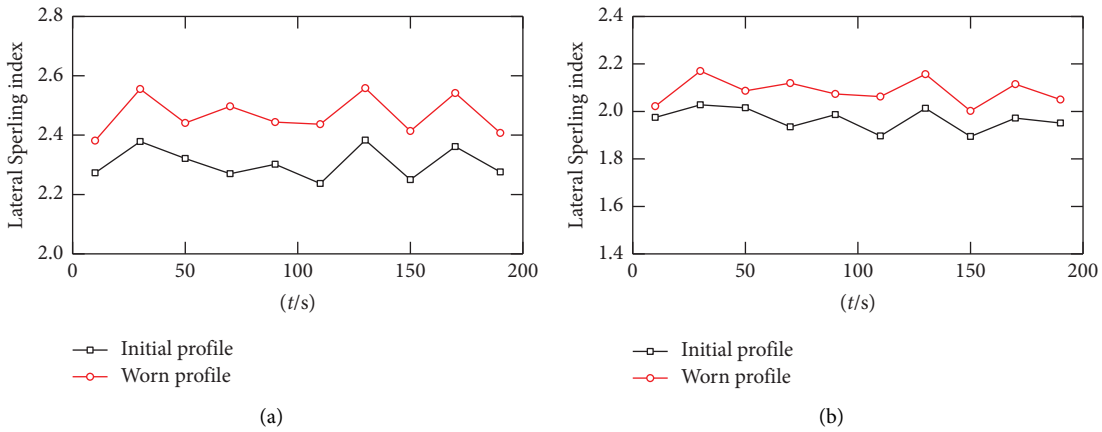

Figure 27: Lateral comfort index of the vehicle before and after wear. (a) Lateral Sperling index at the middle of the vehicle. (b) Lateral Sperling index at the front of the vehicle.

unfavorable wheel-rail contact geometry characteristics, which in turn increases the lateral oscillation of the car body and bogie. Spectrum analysis reveals a significant increase in the 4–8 Hz component in the vehicle's lateral dynamic response, which can seriously affect passenger comfort. To optimize the wheel-rail contact geometry, it is necessary to formulate a wheel reprofile plan based on the wheel's service status during actual operation.

6. Conclusion

This paper carried out a long-term monitoring and data analysis of the wheel and rail profiles on the operating line, then established a wheel wear simulation model based on the wheel-rail interaction and Archard material wear mechanism, and calibrated the model using actual measured data. Finally, based on the simulation model, the wheel wear

evolution under braking conditions and its impact on vehicle dynamic performance were analyzed. The analysis results show the following:

(1) During operation, the wheel mainly undergoes tread concave wear within ±20 mm of the rolling circle. As the running mileage increases, the wear range and depth gradually increase. The average wear depth of the wheel is roughly linear with the operating mileage, and the wear rate is about 0.05 mm/10,000 km. The rail mainly undergoes top surface wear, and the average natural wear rate is about 0.09 mm/year.

(2) The lateral displacement of the wheelset causes a zoning phenomenon in the distribution of contact points and a sudden change in contact geometry parameters for the concave worn profile. When compared with the standard 60 rail profile, the equivalent conicity of the wheel linearly increases with operational mileage. However, when matched with the 60 N rail profile, the wheel's equivalent conicity initially increases and then stabilizes with operational mileage.

(3) Increasing the braking torque from 2 kN·m to 4 kN·m results in nearly twice the wear depth. On straight sections, decreasing the wheel-rail friction coefficient from 0.3 to 0.1 reduces the wear depth by about 23%. On small-radius curve sections, the wheel on the high rail side experiences flange wear, while the wheel on the low rail side experiences tread wear. The use of rail side lubrication reduces the depth of flange wear by approximately 60%.

(4) Concave wear on the wheels leads to unfavorable wheel-rail contact geometry, which increases the lateral oscillation of the car body and bogie. Spectrum analysis reveals a significant increase in the 4~8 Hz component in the vehicle's lateral dynamic response.

Data Availability

No data were used to support the study..

Conflicts of Interest

The authors declare that they have no conflicts of interest in this paper.

Authors' Contributions

Rui Song and Chenxu Lu conceptualised the study. Rui Song curated the data. Lixia Sun investigated the study. Chenxu Lu developed the methodology. Dilai Chen collected the resources. Rui Song and Lixia Sun performed the software analysis. Gang Shen supervised the study. Zhongkai Zhang validated the study. Rui Song wrote the original draft. Chenxu LU wrote, reviewed, and edited the manuscript. The authors have read and agreed to the published version of the manuscript.

Acknowledgments

This research was funded by the project of Shanghai Science and Technology Commission Local Capacity Building, grant no. 22YF1447600: Study on Variable Cross Section Profile Optimization of High-Speed Turnout Oriented to Wear Control; by the key project of Science and Technology Research and Development Plan of China National Railway Group Co., Ltd., grant no. N2022G043: Research on Detection and Evaluation of Rail Wear Profile and Testing Technology under high-speed conditions and grant no. L2022J003: Evaluation Index and Evaluation Method of High-Speed Wheel Tread Concave Grinding; and by the project of China Academy of Railway Science Group Co., Ltd. Research Project, grant no. 2022YJ264: Railway Vehicle Inertial Suspension System and Vibration Reduction Application Research.

References

[1] R. Luo, J. Zeng, H. Y. Dai, and P. B. Wu, "Simulation of wheel wear prediction for high-speed trains," *Tribology*, vol. 29, no. 6, pp. 551–558, 2009.

[2] J. J. Ding, F. Li, and Y. H. Huang, "Analysis of wheel wear model based on creepage mechanism," *China Railway Science*, vol. 31, no. 5, pp. 66–72, 2010.

[3] F. Braghin, R. Lewis, R. S. Dwyer-Joyce, and S. Bruni, "A mathematical model to predict railway wheel profile evolution due to wear," *Wear*, vol. 261, no. 11-12, pp. 1253–1264, 2006.

[4] G. Q. Tao, X. Du, H. J. Zhang, Z. F. Wen, X. S Jin, and D. B. Cui, "Development and validation of a model for predicting wheel wear in high-speed trains," *Journal of Zhejiang University- Science*, vol. 18, no. 8, pp. 603–616, 2017.

[5] A. Orlova and Y. Boronenko, "The influence of the condition of three-piece freight bogies on wheel flange wear: simulation and operation monitoring," *Vehicle System Dynamics*, vol. 48, no. sup1, pp. 37–53, 2010.

[6] Y. Quan Sun, M. Spiryagin, C. Cole, and D. Nielsen, "Wheel–rail wear investigation on a heavy haul balloon loop track through simulations of slow speed wagon dynamics," *Transport*, vol. 33, no. 3, pp. 843–852, 2018.

[7] P. Han and W. H. Zhang, "A new binary wheel wear prediction model based on statistical method and the demonstration," *Wear*, vol. 324, no. 1, pp. 90–99, 2015.

[8] X. S. Jin, Z. F. Wen, X. B. Xiao, and Z. R. Zhou, "A numerical method for prediction of curved rail wear," *Multibody System Dynamics*, vol. 18, no. 4, pp. 531–557, 2007.

[9] X. Yang, Y. Yao, and S. Zhou, "Analysis of the influence of curve super-elevation on rail wear in heavy-haul railway based on modified non-Hertz wheel-rail contact," *Journal of Mechanical Engineering*, vol. 54, no. 4, pp. 93–100, 2018.

[10] X. Li, X. S. Jin, Z. F. Wen, D. B. Cui, and W. H. Zhang, "A new integrated model to predict wheel profile evolution due to wear," *Wear*, vol. 271, no. 1-2, pp. 227–237, 2011.

[11] T. Meinders, P. Meinke, and W. Schiehlen, "Wear estimation in flexible multibody systems with application to railroads," in *Proceedings of the Multibody Dynamics, ECCOMAS Thematic Conference*, pp. 1–20, Madrid, Spain, June 2015.

[12] J. F. Aceituno, P. Wang, L. Wang, and A. A. Shabana, "Influence of rail flexibility in a wheel/rail wear prediction model," *Proceedings of the Institution of Mechanical Engineers, Part F: Journal of Rail and Rapid Transit*, vol. 231, no. 1, pp. 57–74, 2017.

[13] G. Q. Tao, D. X. Ren, L. F. Wang, Z. F. Wen, and X. S. Jin, "Online prediction model for wheel wear considering track flexibility," *Multibody System Dynamics*, vol. 44, no. 3, pp. 313–334, 2018.

[14] S. Hossein-Nia, M. S. Sichani, S. Stichel, and C. Casanueva, "Wheel life prediction model – an alternative to the FASTSIM algorithm for RCF," *Vehicle System Dynamics*, vol. 56, no. 7, pp. 1051–1071, 2018.

[15] R. Luo, H. L. Shi, W. X. Teng, and C. Y. Song, "Prediction of wheel profile wear and vehicle dynamics evolution considering stochastic parameters for high-speed train," *Wear*, vol. 392, pp. 126–138, 2017.

[16] Q. Xiao, B. K. Huang, Y. H. Yang, and C. Chang, "Research on the influence of friction coefficient on wheel-rail wear at high speed," *Journal of the China Railway Society*, vol. 38, no. 4, pp. 39–43, 2016.

[17] X. P. Wang, J. Zhang, and H. Ma, "Prediction method of wheel wear of high speed train," *Tribology*, vol. 38, no. 4, pp. 462–467, 2018.

[18] N. Wilson, H. M. Wu, H. Tournay, and C. Urban, "Effects of wheel/rail contact patterns and vehicle parameters on lateral stability," *Vehicle System Dynamics*, vol. 48, no. sup1, pp. 487–503, 2010.

[19] H. L. Li, F. Li, and Y. Huang, "Research on wheel hollow wear and dynamic performance of freight radial bogies," *Proceedings of the Institution of Mechanical Engineers, Part F: Journal of Rail and Rapid Transit*, vol. 231, no. 9, pp. 1015–1021, 2017.

[20] K. Sawley, C. Urban, and R. Walker, "The effect of hollow-worn wheels on vehicle stability in straight track," *Wear*, vol. 258, no. 7-8, pp. 1100–1108, 2005.

[21] K. Sawley and H. M. Wu, "The formation of hollow-worn wheels and their effect on wheel/rail interaction," *Wear*, vol. 258, no. 7-8, pp. 1179–1186, 2005.

[22] W. J. Lu, G. Q. Tao, P. Wang, Q. Y. Fu, Q. H. Guan, and Z. F. Wen, "Influence of wheel wear on wheel-rail contact characteristics and dynamic performance of metro vehicles," *Engineering Mechanics*, vol. 34, no. 8, pp. 222–231, 2017.

[23] X. S. Jin, G. T. Zhao, S. L. Liang, Z. F. Wen, X. W. Wu, and P. Wang, "Characteristics, mechanisms, influences and counter measures of high speed wheel/rail wear: transverse wear of wheel tread," *Journal of Mechanical Engineering*, vol. 54, no. 4, pp. 3–13, 2018.

[24] M. Ignesti, M. Malvezzi, L. Marini, E. Meli, and A. Rindi, "Development of a wear model for the prediction of wheel and rail profile evolution in railway systems," *Wear*, vol. 284, pp. 1–17, 2012.

[25] M. Ignesti, A. Innocenti, L. Marini, E. Meli, and A. Rindi, "Development of a wear model for the wheel profile optimisation on railway vehicles," *Vehicle System Dynamics*, vol. 51, no. 9, pp. 1363–1402, 2013.

[26] M. Ishida, T. Ban, K. Iida, H. Ishida, and F. Aoki, "Effect of moderating friction of wheel/rail interface on vehicle/track dynamic behaviour," *Wear*, vol. 265, no. 9-10, pp. 1497–1503, 2008.

[27] P. J. Besl and N. D. McKay, "Method for registration of 3-D shapes," *Sensor fusion IV: Control Paradigms and Data Structures*, vol. 1611, pp. 586–606, 1992.

[28] Hot-rolled Steel Rails for railway, "GB/T 2585-2021.2021-03-09," 2021, https://www.chinesestandard.net/PDF/English.aspx/GBT2585-2021.

[29] F. S. Liu, "Study on wheel-rail contact relationship of high speed railway based on wear," *China Railway Science*, vol. 40, no. 3, pp. 38–43, 2019.

[30] M. Hou, G. Yang, B. Chen, and F. S. Liu, "Study on adaptability between service performance of high-speed EMU and rail profile matching," *Journal of the China Railway Society*, vol. 45, no. 5, pp. 29–39, 2023.

[31] W. M. Zhai, K. Y. Wang, and C. B. Cai, "Fundamentals of vehicle–track coupled dynamics," *Vehicle System Dynamics*, vol. 47, no. 11, pp. 1349–1376, 2009.

[32] J. J. Kalker, "A Fast Algorithm for the simplified theory of rolling contact," *Vehicle System Dynamics*, vol. 11, no. 1, pp. 1–13, 2007.

[33] I. Zobory, "Prediction of wheel/rail profile wear," *Vehicle System Dynamics*, vol. 28, no. 2-3, pp. 221–259, 1997.

[34] T. Jendel, "Prediction of wheel profile wear—comparisons with field measurements," *Wear*, vol. 253, no. 1-2, pp. 89–99, 2002.

[35] W. J. Wang, R. Lewis, B. Yang, L. C. Guo, Q. Y. Liu, and M. H. Zhu, "Wear and damage transitions of wheel and rail materials under various contact conditions," *Wear*, vol. 362, pp. 146–152, 2016.